Precisely Regulated In-Plane Pore Sizes of Co-MOF Nanosheet Membranes for Efficient Dye Recovery

Li Wang [a,b,§], Meng Zhang [a,§], Yufei Shu [a], Qi Han [a], Beizhao Chen [a], Bei Liu [a], Zhongying Wang [a,*], Chuyang Y. Tang [b,*]

[a] School of Environmental Science and Engineering, Southern University of Science and Technology, Shenzhen 518055, China

[b] Department of Civil Engineering, The University of Hong Kong, Pokfulam, Hong Kong, China

[§] These two authors contribute equally to this work

* Corresponding authors, wangzy6@sustech.edu.cn; tangc@hku.hk

Abstract

Nanofiltration (NF) is widely used to treat highly saline textile waters, but its efficiency in dye recovery is limited by low permeance. This study presents a novel class of Co-based metal-organic framework (Co-MOF) nanosheet membranes for efficient and selective dye recovery. The Co-MOF membranes have precisely regulated in-plane pore sizes and exhibit superior permeance and selectivity compared to non-porous nanosheet membranes. By adjusting the length of the ligand, the in-plane pore size was precisely tuned from 1.01×0.63 to 1.43 ×0.64 nm^2. The Co-MOF membranes exhibited high selectivity for salts over dye in both diffusion and pressure-driven filtration modes, along with excellent and tunable pure water permeance and high rejection of the dye OII. The remarkable permeability and selectivity of the Co-MOF membranes were attributed to the in-plane pores on the nanosheets, which serve as extra fast “lifts” for water and salts while exhibiting high rejection to the dye molecules. Long-term filtration performance and Co leaching tests demonstrated the stability of the Co-MOF membranes, making them promising candidates for practical dye recovery applications. Overall, this work provides a new approach for the development of high-performance membranes for textile wastewater treatment.

Keywords: 2D Co-MOF; porous nanosheet; layer-stacked membrane; dye recovery; high permeance

1. Introduction

The textile industry in China generates an enormous amount of wastewater, more than 3 billion tons annually [1]. This wastewater is not only highly saline but also poses significant environmental hazards. Discharging it without proper treatment results in a waste of valuable resources [2]. Conventional methods such as adsorption, chemical degradation, and coagulation have proven inadequate for the selective separation and recovery of dyes from saline solutions [3]. However, membrane technology has made significant progress in the treatment of textile wastewater, primarily due to its high energy efficiency and environmentally friendly characteristics [4]. Despite these advantages, commercial polyamide-based nanofiltration (NF) membranes pose a challenge for dye recovery due to their low permeance, typically ~ 10 L m^{-2} h^{-1} bar^{-1}, which limits the efficiency of the process [5-8].

Currently, two-dimensional (2D) layer-stacked membranes utilizing materials such as graphene oxide (GO), molybdenum disulfide (MoS_2), and MXene nanosheets have shown promise in enhancing permselectivity in dye recovery [5, 9-18]. Ma et al. demonstrated a MoS_2/GO membrane that achieved a 5-fold increase in dye/salt selectivity over a commercial loose NF membrane [11]. However, this improvement in selectivity came at the cost of reduced water permeance in these nonporous nanosheet membranes. In layer-stacked membranes, water transport occurs primarily through narrow channels between neighboring nanosheets, leading to increased resistance and reduced water permeance. To address this issue, researchers have attempted to improve water permeance by introducing pores into the nanosheets [19, 20]. For example, Sapkota, *et al*. observed significant enhancements in water fluxes when intrinsic pores were introduced into the nanosheets of MoS_2 membranes using probe sonication [20]. However, methods such as probe sonication and plasma etching cannot precisely control the pore size and often require high energy consumption.

Metal-organic frameworks (MOFs), as a class of porous nanomaterials with a well-ordered microporous structure, have gained considerable research interest and found diverse applications [21-25]. In membrane separation, extensive research has focused on MOF-based mixed matrix composite membranes for gas separation [26, 27]. By precisely tuning the pore size and structure in MOFs, the composite membranes can achieve excellent permeance and selectivity [28]. However, previous studies have predominantly employed MOFs as bulk particles or hybrids within polymer matrices, resulting in potential pore blockage. Additionally, bulk particles are unsuitable for the fabrication of layer-stacked membranes [29, 30]. In contrast, 2D MOF nanosheet membranes are more promising for aqueous membrane separation due to their thin structure and free spacing, which allows for fast molecular transport with reduced resistance [31]. More importantly, the precisely regulatable in-plane pores within the MOF nanosheets can endow the 2D MOF membrane with both improved permeability and high selectivity [32]. The primary strength of the MOF nanosheet membranes, in contrast to alternative porous nanosheet membranes, lies in the straightforward preparation of the MOF nanosheets themselves. In the case of other porous nanosheet membranes, like the porous GO/MXene membranes, additional procedures such as plasma etching, laser etching, or radical oxidation are necessary to establish the intra-plane pores [19, 33, 34]. These methods often entail the use of aggressive chemicals or result in high energy consumption. In sharp contrast, the intra-plane pores are inherently present during the synthesis of the MOF. Despite these outstanding advantages, research on MOF nanosheet membranes for dye wastewater treatment remains limited.

In this study, we report on the facile fabrication of 2D Co-MOF nanosheet membranes with precisely tuned in-plane pore sizes (Fig. 1), which exhibit superior performance in dye recovery. We performed a comprehensive characterization of the Co-MOF membrane structures and accurately calculated their pore sizes. By employing ligands with varying lengths,

77 we precisely tuned the in-plane pore size of Co-MOFs. We systematically tested and evaluated
78 the dye recovery performance of the resulting Co-MOF membranes. We proposed and
79 validated a "lift" transport hypothesis to explain the observed effects. Moreover, we conducted
80 a long-term stability test to demonstrate the excellent durability of Co-MOF membranes,
81 highlighting their great potential for textile wastewater treatment.

82 **2. Materials and methods**

83 **2.1. Chemicals**

84 Cobalt chloride hexahydrate ($CoCl_2 \cdot 6H_2O$, ≥99.99%), benzenedicarboxylic acid (BDC,
85 ≥98%), 2,6-naphthalenedicarboxylic acid (NDC, ≥99%), 4,4'-biphenyldicarbonyl acid (BPDC,
86 ≥97%), triethylamine (TEA, ≥99%) were obtained from Sigma-Aldrich Co. Ltd, America.
87 Poly(vinyl alcohol) (PVA, 67000 Da, AR), sodium chloride (NaCl, ≥99.5%), anhydrous
88 sodium sulfate (Na_2SO_4, ≥99%), magnesium chloride ($MgCl_2$, ≥99%), magnesium sulfate
89 ($MgSO_4$, ≥99%), glucose (≥98%), sucrose (≥99%), dextran (1000 & 2000 Da, AR), orange II
90 sodium salt (OII, ≥85%), Direct Red 80 (DR 80, AR), dimethylformamide (DMF, ≥99.5%)
91 were purchased from McLin Co. Ltd., China. Ultrafiltration (UF) membrane (nylon, 200 nm)
92 was purchased from Jinteng Co. Ltd., China. All chemicals were analytical grade and were
93 used as received without further purification. All solutions were prepared with ultrapure water
94 (Direct 8, Millipore, America).

95 **2.2. Synthesis of the Co-MOFs and the Co-MOF membranes**

96 The Co-MOFs were synthesized following the procedure shown in Fig. 1. Firstly, a
97 mixture of 0.75 mmol of $CoCl_2 \cdot 6H_2O$ and 0.75 mmol of BDC, NDC or BPDC ligands, 2 mL
98 ethanol, 2 mL ultrapure water, and 30 mL DMF were prepared. Next, 0.8 mL of TEA was
99 added and the solution was stirred for 5 min. The mixture was then sonicated in an ultrasonic
100 bath (KQ-300DA, Kunshan, China) at room temperature for 4 h. The resulting bulk Co-MOFs
101 were collected by centrifugation, washed three times with ethanol, and dried at 80 ℃ in a

vacuum oven (DZF-6092, Yiheng, China) for 12 h. Subsequently, 10-50 mg of the bulk Co-MOFs were exfoliated in 50 mL of ultrapure water using probe sonication (Scientz-IID, Xinzhi, China) for 30 min. The resulting nanosheet solution was then poured into a custom-made steel cell (Fig. S1) and deposited onto a UF membrane substrate with a nominal pore size of 200 nm by vacuum filtration under a pressure of 1 bar. The in-plane pore size of the Co-MOFs was precisely tuned by using ligands with different lengths. The resulting Co-MOF membranes were designated as Co-MOF-BDC, Co-MOF-NDC, and Co-MOF-BPDC, corresponding to the respective ligands used in their synthesis.

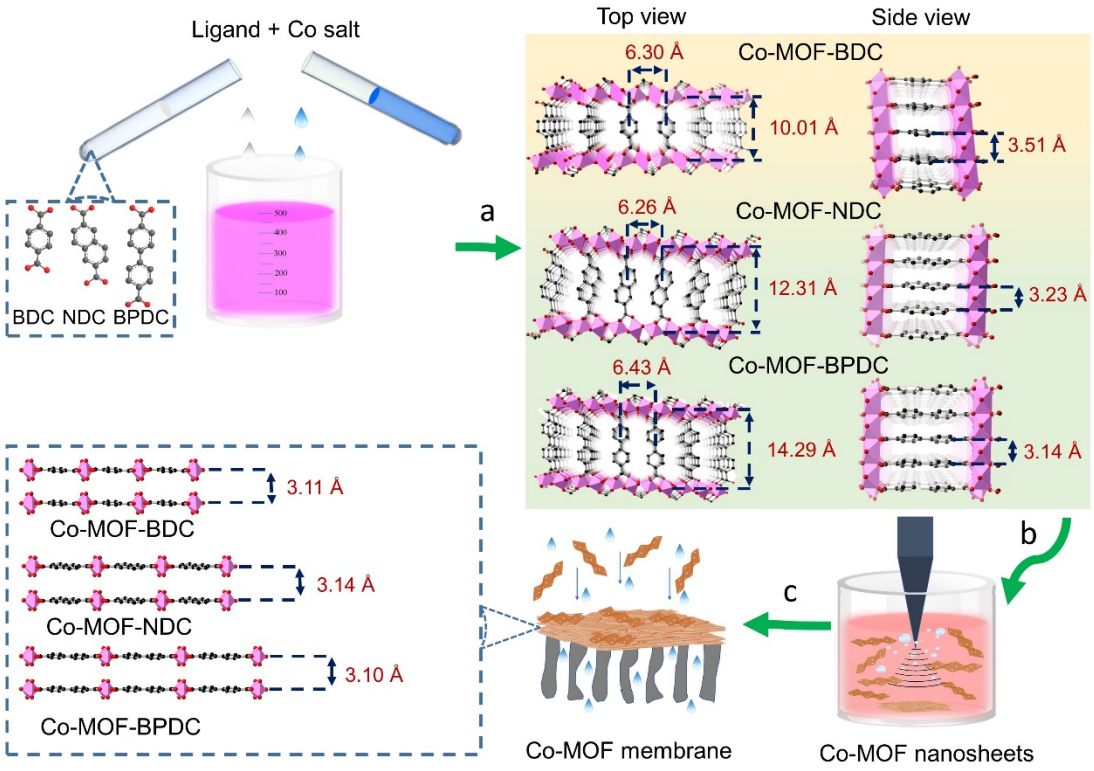

Fig. 1. Schematic illustration of the fabrication process of Co-MOF nanosheets and membranes, including the synthesis of bulk Co-MOF (a), the exfoliation of bulk Co-MOF to obtain Co-MOF nanosheets (b), and the fabrication of the Co-MOF membrane.

2.3. Characterization of Co-MOF nanosheets and membranes

The nanostructure of the Co-MOF nanosheets was obtained by transmission electron microscopy (TEM; Talos F200X G2, Thermo Fisher). The crystal structure information of the Co-MOF nanosheets were obtained by X-ray diffraction (XRD; Smartlab, Rigaku, Japan) with

Cu Kα radiation (λ = 1.5406 Å). X-ray photoelectron spectroscopy (XPS) analysis of the Co-MOF nanosheets was performed with a PHI 5000 Versaprobe III instrument. Fourier transform infrared (FTIR) spectra of the Co-MOF nanosheets were measured using a Nicolet iS50 instrument (Thermo Fisher). The lateral size distribution and zeta potential of the Co-MOF nanosheets were characterized using a Zetasizer Nano ZS instrument (NanoBrook Omini, Brookhaven). The surface morphology and cross-sectional structure of the as-prepared Co-MOF membranes were characterized by scanning electron microscopy (SEM; Merlin, ZEISS, Germany), and the surface roughness was determined by atomic force microscopy (AFM; MFP-3D Stand Alone, Asylum Research).

2.4. Calculation of the pore size of the Co-MOFs

The pore sizes and interlayer spacings of the Co-MOFs were determined by applying Bragg's law ($2d \sin\theta = n\lambda$) [35], where d is the distance between the adjacent lattice planes, θ is the scattering angle, n is an integer determining the reflection order, and λ is the wavelength, which is 1.5406 Å. The sizes for the long side and short side of the in-plane pores were calculated from the scattering angle of the (100) and (010) lattice planes, respectively. Similarly, the interlayer spacings were determined using the scattering angle associated with the (001) lattice planes of both the Co-MOFs and the Co-MOF membranes.

2.5. Membrane performance tests

2.5.1. Pure water permeance test

The pure water permeance of the Co-MOF membranes with various loading amounts (10, 20, 30, and 50 mg) was measured under different pressures ranging from 0.2 to 0.8 bar in a cross-flow cell (Fig. S1). Prior to testing, the Co-MOF membranes were preconditioned for 30 min at the corresponding pressure. Three membrane samples were tested simultaneously, and the error bars were calculated based on the three measurements. The pure water flux was calculated using Equation (1) [36],

$$J_w = \frac{\Delta V}{\Delta t \times A} \quad (1)$$

where Jw (L m^{-2} h^{-1}) is the pure water flux; ΔV (L) is the permeate volume; A (m^2) is the active membrane area; and Δt (h) is the sampling time.

2.5.2. Salt and neutral molecule diffusion test

In the diffusion test, a U-shaped cell with a volume of 100 mL was used. The Co-MOF membrane was placed in the center of the cell and fixed with two clips (Fig. S2). Subsequently, 60 mL of salt solution (NaCl, Na_2SO_4, $MgCl_2$, or $MgSO_4$) with a concentration of 0.25 mol L^{-1} was added to the draw side, while an equal volume of ultrapure water was added to the feed side. The cell was then placed in a water bath at 30 °C and stirred for 6 h. At predetermined time intervals, the salt concentration in the feed solution was determined using a conductivity meter (FE38, FiveEasy plus, Mettler, US). For the neutral molecule diffusion test, 60 mL of 4 g L^{-1} solution of glucose (MW 180.1 Da), sucrose (MW 342.2 Da), dextran 1000 (MW 1000 Da) or dextran 2000 (MW 2000 Da) was added to the draw side, while 60 mL of ultrapure water was added to the feed side. The neutral molecule concentration was measured by a total organic carbon analyzer (TOC, Multi N/C 3100, Analytik Jena AG, Germany). Three membrane samples were tested in parallel for each salt or neutral molecule, and the mean squared error was calculated. Both the salt flux and neutral molecule flux were calculated using Equation (2) [37],

$$J = \frac{\Delta C_f \times V}{\Delta t \times A} \quad (2)$$

where J (mol m^{-2} h^{-1}) is the salt or neutral molecule flux; ΔC_f (mol L^{-1}) is the salt or neutral molecule concentration change in the feed side during the test time; V (L) is the initial volume of the feed side; A (m^2) is the active membrane area; and Δt (h) is the test time.

166 **2.5.3. Salt/dye selective separation performance test**

167 To test the salt/dye selectivity in diffusion, 60 mL of mixed solution containing 1000 mg
168 L^{-1} of NaCl, 1000 mg L^{-1} of Na_2SO_4, and 50 mg L^{-1} of OII was added to the draw side, and 60
169 mL of ultrapure water was added to the feed side. The dye/salt permeance ratio $R_{dye,salt}$ was
170 calculated by Equation (3),

171 $$R_{salt,dye} = \frac{J_{salt}}{J_{dye}} \quad (3)$$

172 where J_{salt} and J_{dye} are the permeances for dye and salt, respectively.

173 To investigate the pressure-dependent performance of the Co-MOF membranes, we tested
174 the salt/dye selectivity under pressure using crosslinked Co-MOF membranes in the crossflow
175 cell. Specifically, 0.2 % PVA was added to a 50 mL Co-MOF nanosheet dispersion and stirred
176 for 30 min to crosslink prior to deposition onto the UF substrate. For the test, the feed solution
177 contained 1000 mg L^{-1} NaCl, 1000 mg L^{-1} Na_2SO_4, and 50 mg L^{-1} OII/DR 80. The system was
178 allowed to run for 2 h without pressure to reach adsorption equilibrium, and then
179 preconditioned at 0.5 bar for 30 min. The dye/salt selectivity $S_{salt,dye}$ was calculated using the
180 following Equation (4) [38],

181 $$S_{salt,dye} = \frac{1-R_{salt}}{1-R_{dye}} \quad (4)$$

182 where R (%) is the dye or salt rejection. The dye and salt rejection was calculated by Equation
183 (5) [36],

184 $$R = \left(1 - \frac{C_p}{C_f}\right) \times 100\% \quad (5)$$

185 where C_p (g L^{-1}) and C_f (g L^{-1}) are the concentrations of the dye and salt in the permeate and
186 feed, respectively.

187 **2.5.4. Stability tests**

188 The long-term filtration stability of the Co-MOF membranes was assessed by conducting
189 a 72-hour cross-flow filtration test under 0.5 bar at pH from 10 to 3, and the water flux was

continuously monitored during the test. To evaluate the leaching of Co ions from the membranes, Co-MOF membranes with a loading of 50 mg were immersed in 50 mL of ultrapure water and shaken at 30°C for 72 h. The concentration of Co ions released from the membranes was then determined using ICP-OES (iCAP 7000 SERIES, Thermo Fisher Scientific, US). Three membrane coupons were tested for each type of Co-MOF membrane at each sampling time, and the average Co leaching value and the root mean square error were calculated.

3. Results and discussion

3.1. Characterization of the Co-MOF nanosheets

After exfoliation of the bulk MOF materials, we characterized the structure, surface properties and chemical components of the Co-MOF nanosheets. TEM images (Fig. 2(a-c)) show rectangular flake profiles of Co-MOF nanosheets with an estimated lateral size of a few hundred nanometers. The AFM images (Fig. 2d-f) reveal the Co-MOF nanosheets to possess an average thickness of about 3 nm. Meanwhile, DLS measurements showed that Co-MOF-BDC, Co-MOF-NDC, and Co-MOF-BPDC had similar hydrodynamic sizes of 1080.00 ± 120.72, 1030.95 ± 85.24 and 897.98 ± 96.60 nm, respectively (Table S1). Additionally, all Co-MOFs exhibited a similar trend in the pH-dependent variation of the zeta potentials (Fig. S3) and showed negative charges in neutral and alkaline solutions due to the residual carboxyl groups in the Co-MOFs [39, 40].

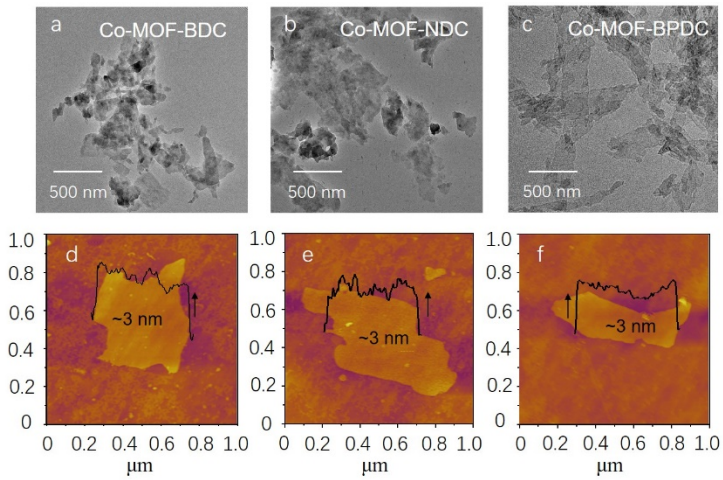

Fig. 2. TEM and AFM images of the Co-MOF-BDC (a, d), Co-MOF-NDC (b, e), and Co-MOF-BPDC (c, f) nanosheets.

XPS survey scans were performed to analyze the O, C, and Co elements in the three Co-MOF nanosheets, as shown in Fig. S5. The concentrations of the O, C and Co were calculated from the survey scan results, and the values are presented in Table S2. Among the Co-MOFs, the Co-MOF-BPDC exhibited the highest concentration of C (69.91%), while the Co-MOF-BDC showed the lowest (59.62%). The high-resolution C 1s XPS spectra of the Co-MOF nanosheets (Fig. 3(a, d, g)) were analyzed, and three major peaks with binding energies at ~284.6, 286.1, and 288.4 eV were identified and assigned to the aromatic ring backbone [34], C-O, and O-C=O groups, respectively [36]. The ratio of the main carbon peaks varied slightly among the three Co-MOFs, which was attributed to the differences in the ligand structures (Table S3 & Fig. S4). The Co 2p XPS spectra (Fig. 3(b, e, h)) showed two main peaks at around 781.0 and 797.1 eV, corresponding to the Co $2p_{3/2}$ and Co $2p_{1/2}$ of Co^{2+}, respectively [41, 42], as well as satellite peaks located at 785.6 and 803.2 eV, also attributed to the Co^{2+} in the three Co-MOFs [43]. In the O 1s XPS spectra (Fig. 3(c, f, i)), the peak at 531.7 eV was assigned to the Co-O-Co coordination bond in the three Co-MOFs, while the peak at 533.0 eV corresponded to the –COOH group of the three ligands (BDC, NDC, and BPDC) [44].

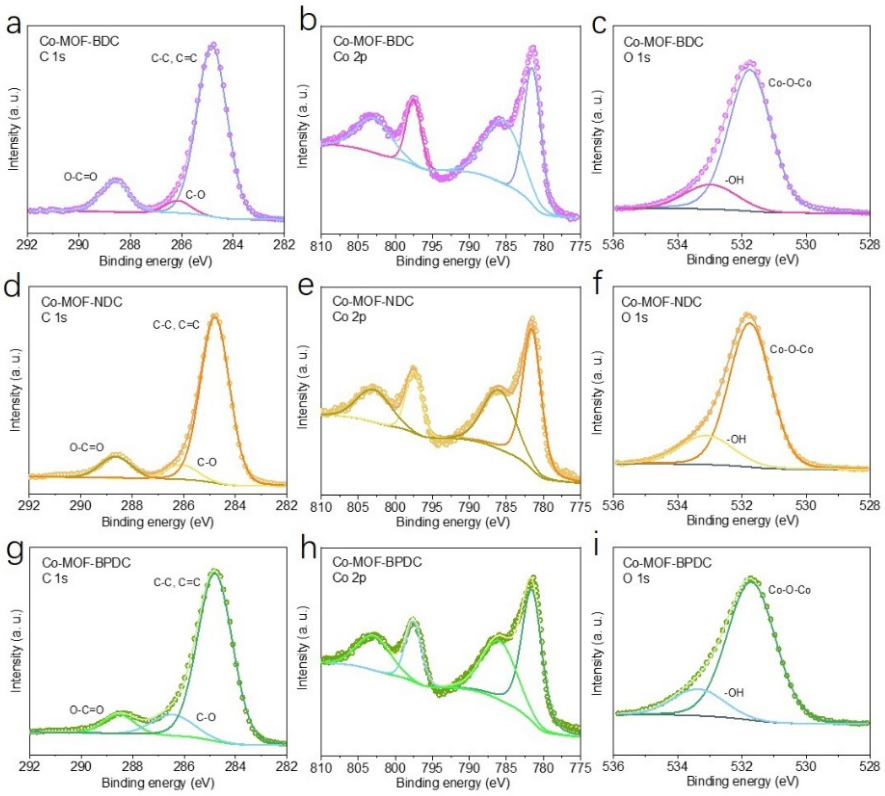

Fig. 3. High-resolution and deconvolution of C 1s, Co 2p and O 1s XPS spectra of the Co-MOF-BDC (a-c), Co-MOF-NDC (d-f), and Co-MOF-BPDC (g-i).

3.2. Characterization of the Co-MOF membranes

The Co-MOF membranes were fabricated by restacking Co-MOF nanosheets onto a UF substrate under an external pressure. The structure of the Co-MOF membranes was analyzed using XRD patterns, and the specific peak positions were determined based on the XRD simulation performed by VESTA, as depicted in Fig. S6. The XRD patterns shown in Fig. 4 indicate that as the ligand length increased from short (BDC) to long (BPDC), the peak for the (100) plane shifted from 8.73° to 6.18°, suggesting an increase in in-plane length from 1.01 nm to 1.43 nm for Co-MOF-BDC and Co-MOF-BPDC, respectively. Furthermore, the peak for the (010) plane was shifted from 14.05° to 13.76°, indicating an increase in in-plane width from 0.63 nm to 0.64 nm for Co-MOF-BDC and Co-MOF-BPDC, respectively, in agreement with previous studies [39, 45]. By adjusting the length of the ligand, the in-plane pore size was precisely tuned from 1.01×0.63 to 1.43×0.64 nm^2. Importantly, the peak for the (001) plane at

28.5° demonstrated similar interlayer spacings of ~0.31 nm for Co-MOF-BDC, Co-MOF-NDC, and Co-MOF-BPDC membranes. These characterizations collectively confirm that Co-MOF membranes with similar interlayer spacing and surface properties have been synthesized, allowing the effect of in-plane size on permselectivity to be investigated.

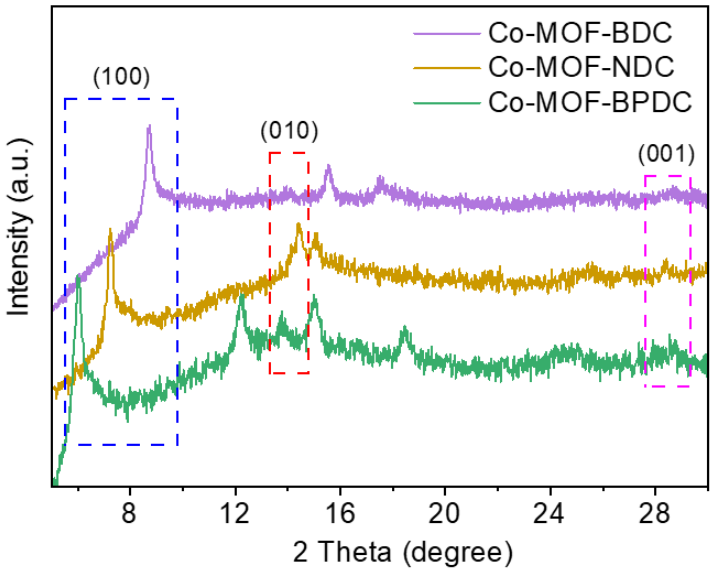

Fig. 4. XRD patterns of the Co-MOF membranes.

The surface morphology and roughness of the Co-MOF membranes were analyzed by AFM. The results, shown in Fig. 5a-c, revealed that the surface roughness of the Co-MOF membranes increased with the length of the ligand, from BDC to BPDC. Specifically, the Co-MOF-BDC membrane had the lowest roughness of 62.0 ± 1.1 nm, while the Co-MOF-BPDC membrane had the highest roughness of 82.3 ± 2.8 nm. This observation could be attributed to the difficulty in exfoliating the Co-MOF-BPDC, which has two aromatic rings, as compared to the other two ligands (Fig. S4). The stronger π-π interaction between adjacent stacked BPDC linkers results in the formation of few-layer nanosheets, leading to more difficult exfoliation and a rougher surface [46-48]. These results suggest that the length of the ligand can influence the surface morphology of the Co-MOF membranes.

The roughness of the Co-MOF membranes may also be influenced by their hydrophilicity. The Co-MOF-BPDC membrane exhibited higher wetting ability with a water contact angle of

51.5°, which was smaller than that of the Co-MOF-NDC membrane at 67.9° (Fig. S7). This may have favored the dispersion of the Co-MOF-BPDC nanosheets in water, resulting in more voids and wrinkles in the orientation of the stacked nanosheets, as reported in previous work [49]. The SEM topographic views of the Co-MOF membranes in Fig. 5(d-f) show an increase in surface roughness from the Co-MOF-BDC to the Co-MOF-BPDC membrane, which is consistent with the observation in the AFM images. The cross-section of the Co-MOF membranes in Fig. 5(g-i) illustrates their well-ordered laminar structure. From the SEM cross-sectional views, the Co-MOF-BDC, Co-MOF-NDC, and Co-MOF-BPDC membranes exhibit estimated thickness values of 7.42 μm, 7.60 μm, and 7.50 μm, respectively. Moreover, the cross-section of the Co-MOF-BDC and Co-MOF-BPDC membranes exhibited more macro voids, which may be due to the collective effect of the exfoliation efficiency and the hydrophilicity of the nanosheets, as discussed above. Fig. 5(j-l) shows the digital photographs of the three Co-MOFs, demonstrating that these membranes were as robust and flexible as other 2D laminar MXene and GO membranes [50-52].

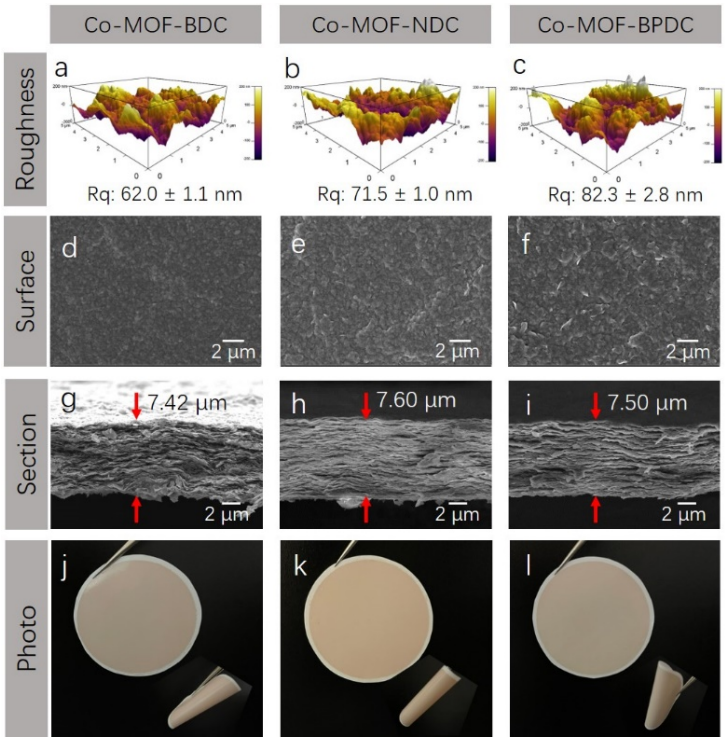

Fig. 5. Surface morphology characterized by AFM images (a-c), surface topography detected by SEM images (d-f), cross-sectional view of the membranes (g-i), and digital photographs (j-l) of the Co-MOF membranes. The thickness of the Co-MOF membranes is marked in the cross-sectional images.

3.3. Performance of the Co-MOF membranes

3.3.1. Effects of loading mass and pressure on water permeance

Fig. 6a presents the measurement of pure water permeance as a function of the deposition amount of Co-MOF nanosheets, ranging from 10 to 50 mg. At a deposition amount of 10 mg, all Co-MOF membranes displayed the highest pure water permeance, with values of 1052 ± 32.0, 541.3 ± 20.8, 368.3 ± 19.8 L m^{-2} h^{-1} bar^{-1} for Co-MOF-BPDC, Co-MOF-NDC, and Co-MOF-BDC membranes, respectively. As the deposition amount increased up to 30 mg, there was a sharp decline in pure water permeance due to the increased membrane thickness and correspondingly higher resistance to water flow. However, further increases in the deposition amount caused only marginal reductions in the pure water permeance. This trend is consistent with the behavior typically observed in 2D membranes, where water permeance decreases with increasing membrane mass or thickness [40, 53, 54]. This phenomenon can be attributed to the highly ordered membrane structure resulting from the complementary stacking of the nanosheets, leading to a stable water permeance. We hypothesize that the stacking structure of the Co-MOF membranes became sufficiently stable at a deposition mass of 30 mg. Therefore, a deposition amount of 30 mg was selected for all subsequent investigations of the Co-MOF membranes.

In Fig. 6, we observed that, at the same loading mass, the pure water permeance of the Co-MOF membranes increased in the order of Co-MOF-BDC < Co-MOF-NDC < Co-MOF-BPDC. This trend, where the pure water permeance increased with the increase of the in-plane pore size (Table S1), highlights the significant role played by the in-plane pores of the Co-MOF nanosheets. By adjusting the length of the ligands (Fig. S4), the in-plane pore size of the Co-MOF membranes can be modulated to increase the effective proportion of the water channels

and thus to reduce the resistance for water molecules to pass through. In nanosheet-stacked membranes, larger in-plane pore sizes also lead to shortened pathways. By reducing the transport distance and the resistance for solvents to pass through the membranes, the membrane permeance can be significantly increased [55, 56]. Furthermore, the pure water flux of the Co-MOF membranes was also measured under varying transmembrane pressure (Fig. 6b). As the pressure increased from 0.2 bar to 0.8 bar, all three Co-MOF membranes displayed a four-fold increase in pure water flux. The linear increase in pure water flux with increasing driving pressure for the three Co-MOF membranes indicates their structural stability [57, 58]. Co-MOF membranes with different loading mass also showed a similar linear trend in pure water flux with increasing driving pressure, as shown in Fig. S8. To determine the average pore size of the Co-MOF membranes, we employed MWCO method, which describes the molecular weight corresponding to a 90% rejection [59]. Accordingly, from the results shown in Fig. S9, it is evident that the MWCO of Co-MOF-BDC, Co-MOF-NDC, and Co-MOF-BPDC were identified as ~1000 Da, ~1600 Da, and ~2000 Da, respectively.

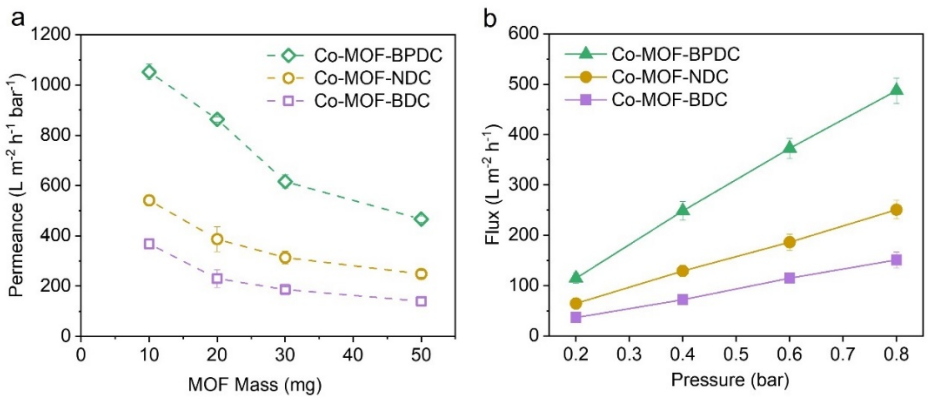

Fig. 6. The pure water permeance of Co-MOF membranes fabricated with varied masses (a) and pure water flux under different transmembrane pressure (b)

3.3.2. Salt/dye selective separation performance of the Co-MOF membranes

The Co-MOF membranes were tested for their separation performance in both diffusion mode and pressure-driven mode, as shown in Fig. 7. Four different salts, NaCl, $MgCl_2$, Na_2SO_4,

and $MgSO_4$, were used to evaluate the salt diffusion performance of the Co-MOF membranes. The diffusion permeance was found to follow the order of NaCl > $MgCl_2$ > Na_2SO_4 > $MgSO_4$ for all three Co-MOF membranes (Fig. 7a). This order is likely due to the combined effect of steric hindrance and Donnan exclusion. Due to its larger hydrated ion radius (Na^+: 0.358 nm, Mg^{2+}: 0.428 nm), Mg^{2+} encountered greater steric hindrance when entering and diffusing through the pores of the Co-MOF membranes, while the Co-MOF membranes were negatively charged around neutral pH (Fig. S3), leading to stronger repulsion toward higher valence anions (i.e., SO_4^{2-} > Cl^-) [20]. Notably, the salt permeance generally increased with the in-plane pore size of the Co-MOF membranes, with Co-MOF-BPDC membrane showing the highest salt diffusion permeance among the three membranes for all four salts tested, at 2.9 ± 0.2, 1.5 ± 0.1, 1.3 ± 0.1 and 1.0 ± 0.1 mol m^{-2} h^{-1} for NaCl, $MgCl_2$, Na_2SO_4, and $MgSO_4$, respectively. In comparison, the reported permeances of GO membranes were only 2.7 × 10^{-2}, 2.3 × 10^{-2} and 1.7 × 10^{-2} mol m^{-2} h^{-1} for NaCl, $MgCl_2$ and $CaCl_2$, respectively [60]. The high salt permeance of the Co-MOF membranes was attributed to the extra "lifts" in the nanosheets, which shortened the transport distance and resistance for salts passing through the membranes.

The Co-MOF membranes were also evaluated for their organic solute separation performance using four neutral molecules with distinct molecular weights (Table S4) [61]. The diffusion permeance of these molecules, including glucose, sucrose, dextran 1000, and dextran 2000, generally increased with the in-plane pore size of the Co-MOF membranes (Fig. 7b). In particular, the Co-MOF-BPDC membrane with the largest in-plane pore size exhibited the highest diffusion permeance for all four molecules. Additionally, for a specific Co-MOF membrane, the diffusion permeance of neutral molecules followed the sequence of glucose > sucrose > dextran 1000 > dextran 2000, as larger molecules experienced greater steric hindrance in passing through the membranes.

To evaluate the potential of Co-MOFs in dye recovery applications, their salt/dye separation performance was investigated using both diffusion- and pressure-driven filtration modes (Fig. 7c and Fig. 7d, respectively). In the diffusion mode, all the Co-MOF membranes exhibited high selectivity for salts over dyes. Specifically, the Co-MOF-BDC membrane showed permeance ratios of 74.0 ± 6.1 and 43.7 ± 3.3 for NaCl/OII and Na_2SO_4/OII, respectively. These ratios increased to 81.4 ± 3.1 and 58.6 ± 1.5, respectively, for the Co-MOF-BPDC membrane with the largest in-plane pore size. The higher salt/dye permeance ratio observed in the Co-MOF-BPDC membrane can be attributed to the increased in-plane pore size and decreased negative charge density, which allowed for reduced rejection to salts while maintaining a similarly large steric hindrance to the dye. Therefore, the salt/dye permeance ratio increased with the enlarged in-plane pore size of the Co-MOF membranes.

To evaluate the dye recovery performance under pressure, the Co-MOF membranes were tested as shown in Fig. 7d. The Co-MOF-BDC membrane with the smallest in-plane pore size exhibited the highest rejections against salts and dye, with rejection values of 9.07 ± 0.2 %, 18.9 ± 2.1 %, and 95.8 ± 3.2 % for NaCl, Na_2SO_4, and OII, respectively. This resulted in selectivity values of 21.9 and 19.5 for NaCl/OII and Na_2SO_4/OII, respectively. Given the pronounced selectivity our Co-MOF membranes demonstrated between salts and smaller dyes, it is reasonable to anticipate an even greater selectivity between salts and dyes with larger molecular weight. To verify this hypothesis, we performed an additional test using a dye with a higher molecular weight (DR 80, 1373.07 Da). Notably, as depicted in Fig. S10, our Co-MOF-BDC membrane showed high selectivity values of 54.7 and 48.6 for NaCl/DR 80 and Na_2SO_4/DR 80, respectively. However, the selectivity values decreased with the increased in-plane pore size of the Co-MOF membranes. A discernible disparity emerges in in dye/salt selectivity of the Co-MOF membranes when tested through diffusion and pressure-driven modes. This intriguing variation can be potentially attributed to the distinctive dominating

effect. In the context of diffusion, the mass transfer of dye molecules was dominated by the steric hindrance effect and Donnan exclusion provided by the pores of the Co-MOFs. In contrast, the pressure-driven process instigates a contrasting dynamic, particularly in Co-MOF membranes with larger pore sizes. Dye molecules could be more easily compelled to traverse through the large pores by the pressure. As a result, the dye/salt permeance ratio exhibits an increase in the pressure-driven mode, particularly in comparison with the diffusion mode, leading to a reduction in the selectivity for Co-MOF membranes with larger pores.

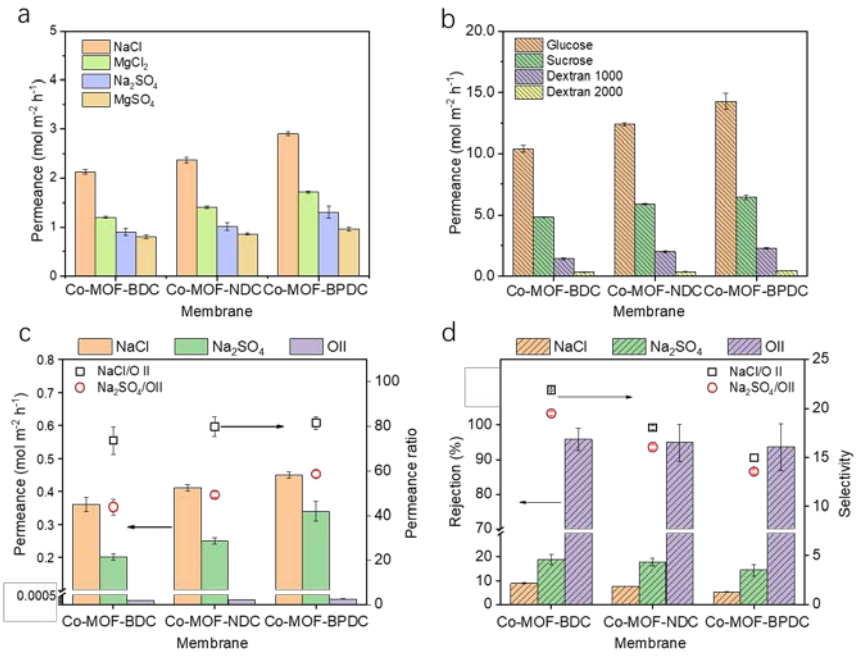

Fig. 7. Diffusion performance for salts and neutral molecules, and dye recovery of the three Co-MOF membranes: salt diffusion performance (a), neutral molecule diffusion (b), dye recovery in diffusion (c), and dye recovery under pressure (d).

The dye recovery performance of the Co-MOF membranes was compared with that of other laminar membranes reported in the literature (Table 1). The Co-MOF membranes demonstrated excellent and tunable pure water permeance in the range of 186.7 ± 11.5 to 615.8 ± 26.4 L m^{-2} h^{-1} bar^{-1}, which was 2 – 60 times higher than that of non-porous laminar membranes. Meanwhile, the Co-MOF membranes exhibited the highest rejection against OII of 95.8 ± 3.2 % with a low rejection to NaCl at 5.4 ± 0.3 %, which is comparable to the

previously reported performance (Table 1). Therefore, our Co-MOF membranes exhibit great potential for dye recovery with high efficiency.

The porous Co-MOF nanosheet membranes exhibit significantly higher permeance than that of the non-porous nanosheet membranes as reported in previous studies [11, 16, 45]. A schematic figure (Fig. 8) illustrates the transport mechanism underlying the exceptional permeance and selectivity of the porous Co-MOF membranes with precisely regulated in-plane pore sizes. In non-porous membranes such as GO membranes, water molecules and salts are transported transversely through the confined nanochannels between adjacent nanosheets [62, 63]. This results in limited permeance due to significant transport resistance and distance [64]. In contrast, the in-plane pores in our Co-MOF membranes with precisely tuned pore sizes act as “lifts” with low transport resistance, allowing water and salts to pass through more straightforwardly. Regarding the “lifts”, denoting the intra-plane pores, their hydrophilic and negatively charged surface properties confer them the capacity to selectivity differentiate between the negatively charged dye molecules and water molecules, resulting in excellent dye rejection and enhanced water permeability. Taking advantage of this, the pure water permeance of the Co-MOF membranes is at least 3 times higher than that of non-porous nanosheet membranes with a comparable thickness (up to 200 L m^{-2} h^{-1} bar^{-1}) [16]. Furthermore, by adjusting the length of the ligands for the Co-MOFs, the in-plane pore size can be tuned to fabricate a wider range of Co-MOF membranes with excellent water permeance and precise selectivity.

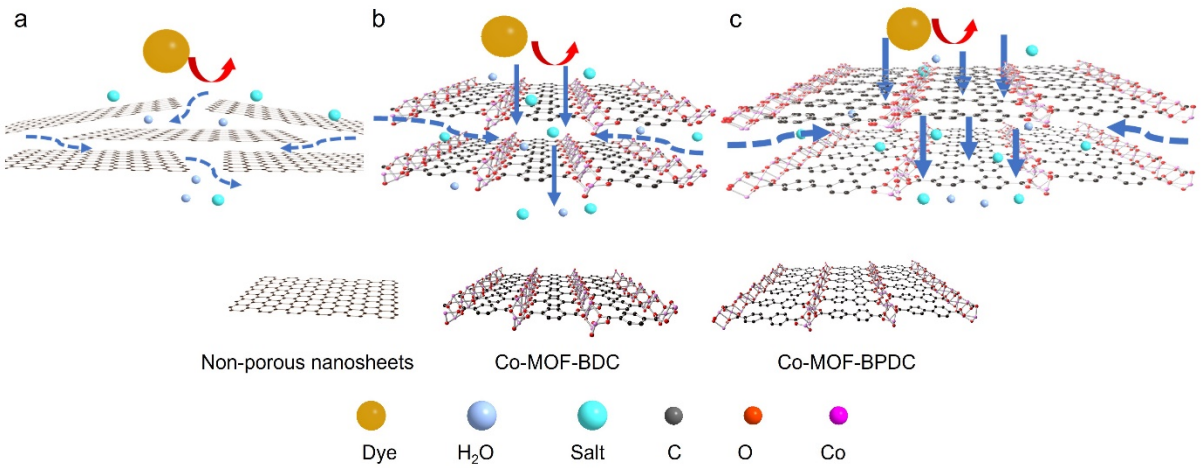

Fig. 8. The separation mechanism of stacked membranes prepared with (a) non-porous nanosheet membrane, Co-MOF membranes with small (b) and large (c) in-plane pores.

Table 1. Comparison of membrane performance of this study with literature work.

Membrane	Dye/salt	Salt/dye selectivity	Permeance ($L\ m^{-2}\ h^{-1}\ bar^{-1}$)	Ref.
Co-MOF-BDC	NaCl/OII	21.9 ± 0.1	186.7 ± 11.5	This work
	Na_2SO_4/OII	19.5 ± 0.2		
	NaCl/ DR 80	54.7 ± 0.1		
	Na_2SO_4/DR 80	48.6 ± 0.2		
Co-MOF-NDC	NaCl/OII	18.1 ± 0.2	313.8 ± 25.1	This work
	Na_2SO_4/OII	16.0 ± 0.2		
	NaCl/ DR 80	45.8 ± 0.3		
	Na_2SO_4/DR 80	42.3 ± 0.3		
Co-MOF-BPDC	NaCl/OII	15.0 ± 0.3	615.8 ± 26.4	This work
	Na_2SO_4/OII	13.6 ± 0.2		
	NaCl/ DR 80	42.6 ± 0.3		
	Na_2SO_4/DR 80	39.4 ± 0.3		
MXene	NaCl/CR	25.1	195.3 ± 6.5	[5]
MoS_2/GO	Na_2SO_4/CR*	110	48.27	[11]

c-GO/PAN	Na_2SO_4/DR 80	54	112	[38]
rGO	Na_2SO_4/MB	> 38.0	80	[65]
PRGO	Na_2SO_4/RB 5	40.8	11.3	[66]

* Data interpreted from literature.

3.4. The long-term stability of the Co-MOF membranes

To evaluate the long-term stability of the Co-MOF membranes for practical applications, we conducted a 72-h assessment of their filtration performance under different pH conditions. As is evident in Fig. 9, the water permeance for the Co-MOF-BDC, Co-MOF-NDC, and Co-MOF-BPDC membranes remained steady, maintaining at ~180, ~320, and ~620 L m^{-2} h^{-1} bar^{-1}, respectively, across the pH range from 5 to 10. Meanwhile, the rejection for the Co-MOF-BDC, Co-MOF-NDC, and Co-MOF-BPDC membranes also exhibited a persistent trend at 96.7%, 95.8%, and 94.5%, respectively. This noteworthy constancy across the three Co-MOF membranes stands out as a testament to their excellent stability. However, when the pH value decreased to 3, a significant increase in water permeance was observed, accompanied with a dramatic decrease in rejection across all three Co-MOF membranes.

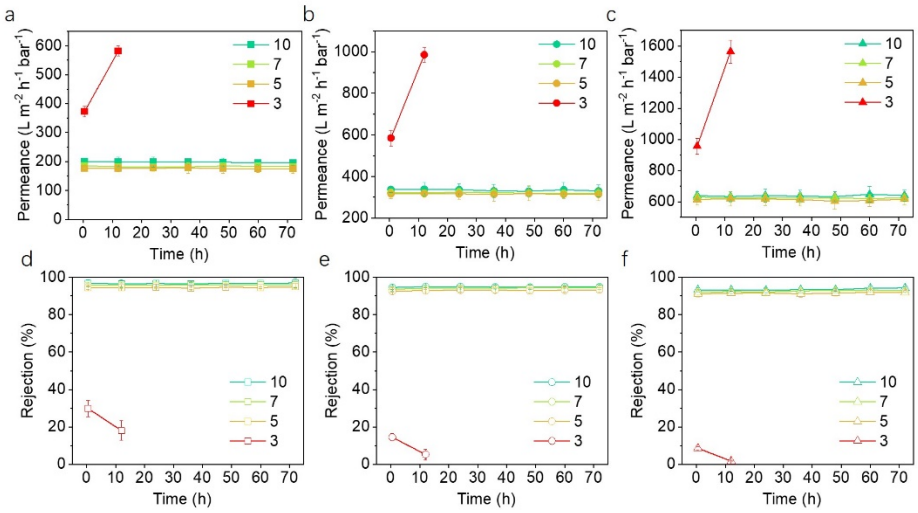

Fig. 9. Water permeance (a, b, and c) and rejection (d, e, and f) against OII for the Co-MOF-BDC, Co-MOF-NDC and Co-MOF-BPDC membranes, respectively.

To investigate the structural stability of the Co-MOF membranes, the XRD patterns were examined after 72-h of filtration under distinct pH conditions. The results, illustrated in Fig. S11, bear testimony to the endurance of the peaks corresponding to (100), (010), and (001) planes for the three Co-MOF membranes when exposed to pH 7 and 10, thereby demonstrating the structural stability of the Co-MOF membranes under these pH conditions. However, these peaks exhibited weakened or became vanishing at pH 3, underscoring the structural damage under a harsh acidic condition.

Furthermore, XPS survey scans were performed after 72-h, as shown in Fig. S12 and Table S(5-7). The initial atomic percentage of Co was 11.95%, 9.18%, and 7.14% for Co-MOF-BDC, Co-MOF-NDC, and Co-MOF-BPDC membranes, respectively. After 72-h filtration, these atomic percentages of Co displayed minimal change at pH 7 and 10, indicating the stability of the Co-MOF membranes. Notably, at pH 3, these percentages decreased to 6.87%, 3.37%, and 2.36%, respectively, because of the Co leaching from the surface fragments of the Co-MOF nanosheets under acidic conditions. High-resolution O 1s XPS spectra were examined for the three Co-MOF membranes after 72-h filtration (Fig. 10), and the content of the O-Co-O coordination bond was calculated as detailed in Table S8 for the purpose of comparison. The initial contents of the O-Co-O coordination bond were 89.85%, 83.68%, and 78.81% for Co-MOF-BDC, Co-MOF-NDC and Co-MOF-BPDC membrane, respectively. After 72-h, these values did not change significantly at pH 7 and 10. For instance, the content of O-Co-O coordination bond exhibited similar values at 88.83%, 82.79%, and 78.78% at pH 7, respectively, indicating the stability of the Co-MOF membranes. However, at pH 3, these values decreased to 45.67%, 34.84%, and 28.59%, respectively, due to the inherent instability of the coordination bond (O-Co-O) under such harsh pH conditions.

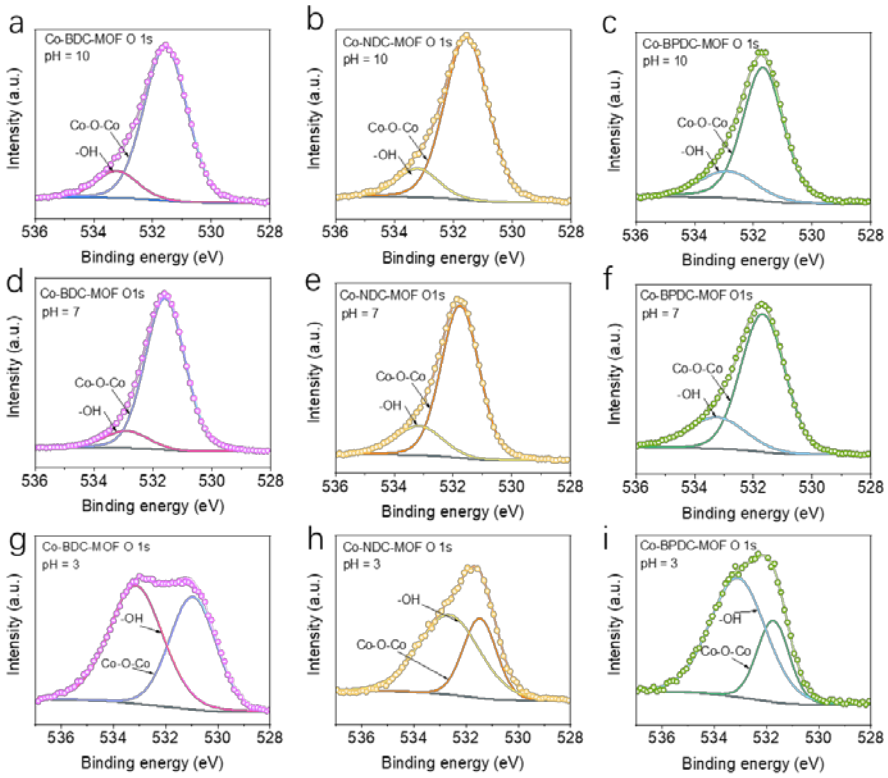

Fig. 10. High-resolution O 1s XPS spectra of the Co-MOF-BDC (a, d, g), Co-MOF-NDC (b, e, h), and Co-MOF-BPDC (c, f, i) membranes after 72-h filtration under different pH conditions.

TEM images were examined to observe the variation in morphology of the Co-MOF nanosheets after 72-h filtration under different pH conditions, as shown in Fig. 11. Evidently, the profiles of nanosheets for three Co-MOF membranes remained unchanged at pH 7 and 10, indicating their structural stability. However, a slight decline in the lateral size of the nanosheets and a blurred profile were observed at pH 3, attributable to the rupture of the O-Co-O coordination bonds at this condition.

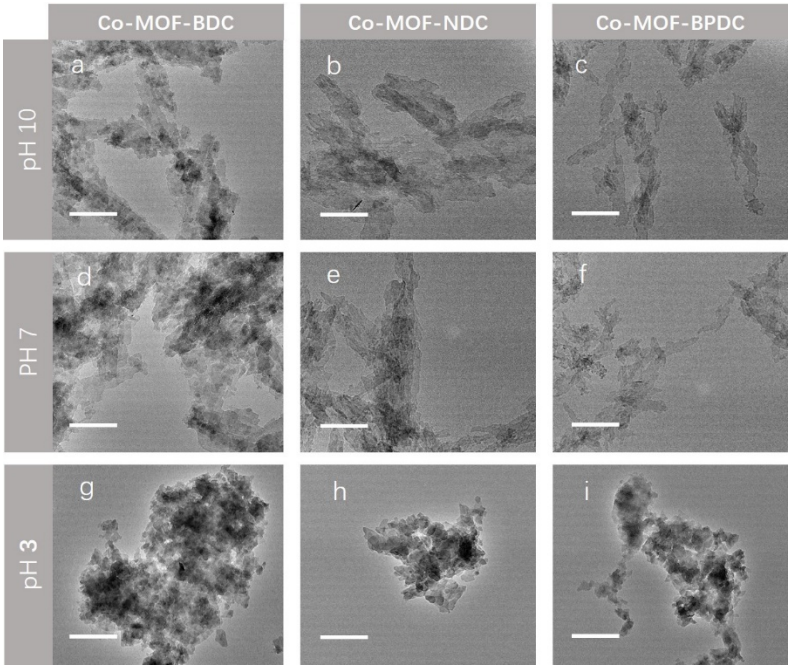

Fig. 11. TEM images of the Co-MOF-BDC (a, d, g), Co-MOF-NDC (b, e, h), and Co-MOF-BPDC (c, f, i) nanosheets after 72-h filtration under different pH conditions.

During the exfoliation process, fragments were generated by ultrasonic energy at the edge of the Co-MOF nanosheets. This process leads to the potential leaching of a small amount of Co from the remaining fragments during the filtration process. As such, a 72-h assessment of the Co leaching was conducted. As shown in Fig. S13, it plateaued within the first 36 hours at approximately 0.8 mg L^{-1}, which is below the wastewater effluent standard of 1 mg L^{-1} [67]. After 72 hours, the Co leaching only accounted for 2.11 ± 0.03 %, 1.49 ± 0.02 %, and 2.19 ± 0.03 % of the total Co mass for Co-MOF-BDC, Co-MOF-NDC, and Co-MOF-BPDC membranes, respectively. These results demonstrate the exceptional long-term stability of our Co-MOF membranes in both filtration performance and structure, indicating their potential for practical applications.

4. Conclusions

In summary, we have successfully fabricated a series of Co-MOF nanosheet membranes with precisely regulated in-plane pore sizes and evaluated their potential for dye recovery application. The Co-MOF membranes exhibited excellent water permeance and selectivity, as well as high rejections to OII while maintaining low rejections to NaCl and Na_2SO_4. Particularly, the Co-MOF-BPDC membrane with the largest in-plane pore size showed the highest pure water permeance of 615.8 ± 26.4 L m^{-2} h^{-1} bar^{-1} and excellent selectivity for NaCl/OII and Na_2SO_4/OII at 15.0 and 13.6, respectively. Compared to the non-porous 2D nanosheet membranes in which the molecular transport follows tortuous nanochannel pathways between the adjacent nanosheets, the porous Co-MOF membranes contain in-plane pores with tunable sizes as additional "lifts" for water and salt permeance. Consequently, the Co-MOF-BPDC membrane exhibited excellent water permeance (at least 3 times higher than that of the non-porous nanosheet membranes and 60 times higher than the commercial NF90 membrane) and comparative salt/dye selectivity. Moreover, the Co-MOF membranes showed long-term stability in both filtration performance and structure, as well as low Co leaching rate. These results demonstrate that our Co-MOF membranes have great potential for practical dye recovery applications, and the precisely regulated in-plane pore sizes provide a promising strategy for the design and fabrication of advanced separation membranes with superior performance.

Acknowledgments

This research was supported by the National Natural Science Foundation of China (No. 22076075), the Stable Support Plan Program of Shenzhen Natural Science Fund (No. 20200925155303001), SUSTech-MIT Joint Center for Mechanical Engineering Education and Research. The authors acknowledge the assistance of SUSTech Core Research Facilities.

References

[1] Y.F. Mi, N. Wang, Q. Qi, B. Yu, X.D. Peng, Z.H. Cao, A loose polyamide nanofiltration membrane prepared by polyether amine interfacial polymerization for dye desalination, Sep. Purif. Technol. 248 (2020) 117079. https://doi.org/https://doi.org/10.1016/j.seppur.2020.117079.

[2] S. Liu, Z. Wang, M. Ban, P. Song, X. Song, B. Khan, Chelation–assisted in situ self-assembly route to prepare the loose PAN–based nanocomposite membrane for dye desalination, J. Membr. Sci. 566 (2018) 168-180. https://doi.org/https://doi.org/10.1016/j.memsci.2018.09.002.

[3] S. Liu, Z. Wang, P. Song, Free radical graft copolymerization strategy to prepare catechin-modified chitosan loose nanofiltration (NF) membrane for dye desalination, ACS Sustain. Chem. Eng. 6(3) (2018) 4253-4263. https://doi.org/10.1021/acssuschemeng.7b04699.

[4] W.-J. Lau, A.F. Ismail, Polymeric nanofiltration membranes for textile dye wastewater treatment: Preparation, performance evaluation, transport modelling, and fouling control — a review, Desalination 245(1) (2009) 321-348. https://doi.org/https://doi.org/10.1016/j.desal.2007.12.058.

[5] Y. Li, R. Dai, H. Zhou, X. Li, Z. Wang, Aramid nanofiber membranes reinforced by Mxene nanosheets for recovery of dyes from textile wastewater, ACS Appl. Nano Mater. 4(6) (2021) 6328-6336. https://doi.org/10.1021/acsanm.1c01217.

[6] H. Zhang, L. Bin, J. Pan, Y. Qi, J. Shen, C. Gao, B. Van der Bruggen, Carboxyl-functionalized graphene oxide polyamide nanofiltration membrane for desalination of dye solutions containing monovalent salt, J. Membr. Sci. 539 (2017) 128-137. https://doi.org/10.1016/j.memsci.2017.05.075.

[7] C.L. Ritt, T. Stassin, D.M. Davenport, R.M. DuChanois, I. Nulens, Z. Yang, A. Ben-Zvi, N. Segev-Mark, M. Elimelech, C.Y. Tang, G.Z. Ramon, I.F.J. Vankelecom, R. Verbeke, The open membrane database: Synthesis–structure–performance relationships of reverse osmosis membranes, J. Membr. Sci. 641 (2022) 119927. https://doi.org/https://doi.org/10.1016/j.memsci.2021.119927.

[8] Z. Yang, H. Guo, C.Y. Tang, The upper bound of thin-film composite (TFC) polyamide membranes for desalination, J. Membr. Sci. 590 (2019). https://doi.org/10.1016/j.memsci.2019.117297.

[9] F. Wu, Y. Liu, G. Yu, D. Shen, Y. Wang, E. Kan, Visible-light-absorption in graphitic C_3N_4 bilayer: Enhanced by interlayer coupling, J. Phys. Chem. Lett. 3(22) (2012) 3330-3334. https://doi.org/10.1021/jz301536k.

[10] Y. Wang, B. Gao, Q. Yue, Z. Wang, Graphitic carbon nitride (g-C_3N_4)-based membranes for advanced separation, J. Mater. Chem. A 8(37) (2020) 19133-19155. https://doi.org/10.1039/d0ta06729f.

[11] J. Ma, X. Tang, Y. He, Y. Fan, J. Chen, HaoYu, Robust stable MoS_2/GO filtration membrane for effective removal of dyes and salts from water with enhanced permeability, Desalination 480 (2020). https://doi.org/10.1016/j.desal.2020.114328.

[12] Z. Wang, Q. Tu, A. Sim, J. Yu, Y. Duan, S. Poon, B. Liu, Q. Han, J.J. Urban, D. Sedlak, B. Mi, Superselective removal of lead from water by two-dimensional MoS_2 nanosheets and layer-stacked membranes, Environ. Sci. Technol. 54(19) (2020) 12602-12611. https://doi.org/10.1021/acs.est.0c02651.

[13] Z. Wang, A. Sim, J.J. Urban, B. Mi, Removal and recovery of heavy metal ions by two-dimensional MoS_2 nanosheets: Performance and mechanisms, Environ. Sci. Technol. 52(17) (2018) 9741-9748. https://doi.org/10.1021/acs.est.8b01705.

[14] X. Wu, M. Ding, H. Xu, W. Yang, K. Zhang, H. Tian, H. Wang, Z. Xie, Scalable $Ti_3C_2T_x$ Mxene interlayered forward osmosis membranes for enhanced water purification and organic solvent recovery, ACS Nano 14(7) (2020) 9125-9135. https://doi.org/10.1021/acsnano.0c04471.

[15] L. Ding, D. Xiao, Z. Lu, J. Deng, Y. Wei, J. Caro, H. Wang, Oppositely charged $Ti_3C_2T_x$ MXene membranes with 2D nanofluidic channels for osmotic energy harvesting, Angew. Chem. Int. Ed. 59(22) (2020) 8720-8726. https://doi.org/10.1002/anie.201915993.

[16] Y. Kang, Y. Xia, H. Wang, X. Zhang, 2D laminar membranes for selective water and ion transport, Adv. Funct. Mater. 29(29) (2019). https://doi.org/10.1002/adfm.201902014.

[17] J. Ran, P. Zhang, C. Chu, P. Cui, X. Ai, T. Pan, Y. Wu, T. Xu, Ultrathin lamellar MoS_2 membranes for organic solvent nanofiltration, J. Membr. Sci. 602 (2020) 117963. https://doi.org/https://doi.org/10.1016/j.memsci.2020.117963.
[18] S. Cao, A. Deshmukh, L. Wang, Q. Han, Y. Shu, H.Y. Ng, Z. Wang, J.H. Lienhard, Enhancing the permselectivity of thin-film composite membranes interlayered with MoS_2 nanosheets via precise thickness control, Environ. Sci. Technol. 56(12) (2022) 8807-8818. https://doi.org/10.1021/acs.est.2c00551.
[19] Y. Yang, X. Yang, L. Liang, Y. Gao, H. Cheng, X. Li, M. Zou, R. Ma, Q. Yuan, X. Duan, Large-area graphene-nanomesh/carbon-nanotube hybrid membranes for ionic and molecular nanofiltration, Science 364(6445) (2019) 1057-1062.
[20] B. Sapkota, W. Liang, A. VahidMohammadi, R. Karnik, A. Noy, M. Wanunu, High permeability sub-nanometre sieve composite MoS_2 membranes, Nat. Commun. 11(1) (2020) 2747. https://doi.org/10.1038/s41467-020-16577-y.
[21] H. Deng, C.J. Doonan, H. Furukawa, R.B. Ferreira, J. Towne, C.B. Knobler, B. Wang, O.M. Yaghi, Multiple functional groups of varying ratios in metal-organic frameworks, Science 327(5967) (2010) 846-850.
[22] Introduction to metal–organic frameworks, Chem. Rev. 112(2) (2012) 673-674. https://doi.org/10.1021/cr300014x.
[23] D.B. Shinde, G. Sheng, X. Li, M. Ostwal, A.H. Emwas, K.W. Huang, Z. Lai, Crystalline 2D covalent organic framework membranes for high-flux organic solvent nanofiltration, Journal of the American Chemical Society 140(43) (2018) 14342-14349. https://doi.org/10.1021/jacs.8b08788.
[24] W. Li, P. Su, Z. Li, Z. Xu, F. Wang, H. Ou, J. Zhang, G. Zhang, E. Zeng, Ultrathin metal–organic framework membrane production by gel–vapour deposition, Nat. Chem. 8(1) (2017) 406. https://doi.org/10.1038/s41467-017-00544-1.
[25] Z. Wang, D. Wang, S. Zhang, L. Hu, J. Jin, Interfacial design of mixed matrix membranes for improved gas separation performance, Adv. Mater. 28(17) (2016) 3399-3405. https://doi.org/https://doi.org/10.1002/adma.201504982.
[26] R. Li, Z. Wang, Z. Yuan, C. Van Horne, V. Freger, M. Lin, R. Cai, J. Chen, A comprehensive review on water stable metal-organic frameworks for large-scale preparation and applications in water quality management based on surveys made since 2015, Crit. Rev. Environ. Sci. Technol. 52(22) (2022) 4038-4071.
[27] H. Daglar, I. Erucar, S. Keskin, Recent advances in simulating gas permeation through MOF membranes, Mater. Adv. 2(16) (2021) 5300-5317. https://doi.org/10.1039/D1MA00026H.
[28] D.L. Zhao, F. Feng, L. Shen, Z. Huang, Q. Zhao, H. Lin, T.-S. Chung, Engineering metal–organic frameworks (MOFs) based thin-film nanocomposite (TFN) membranes for molecular separation, Chem. Eng. J. 454 (2023) 140447. https://doi.org/https://doi.org/10.1016/j.cej.2022.140447.
[29] X. Zhang, H. Li, J. Wang, D. Peng, J. Liu, Y. Zhang, In-situ grown covalent organic framework nanosheets on graphene for membrane-based dye/salt separation, J. Membr. Sci. 581 (2019) 321-330. https://doi.org/10.1016/j.memsci.2019.03.070.
[30] Y. Wen, X. Zhang, X. Li, Z. Wang, C.Y. Tang, Metal–organic framework nanosheets for thin-film composite membranes with enhanced permeability and selectivity, ACS Appl. Nano Mater. 3(9) (2020) 9238-9248. https://doi.org/10.1021/acsanm.0c01860.
[31] Y. Peng, W. Yang, 2D metal-organic framework materials for membrane-based separation, Adv. Mater. Interfaces 7(1) (2020) 1901514. https://doi.org/https://doi.org/10.1002/admi.201901514.
[32] Y. Feng, Z. Wang, W. Fan, Z. Kang, S. Feng, L. Fan, S. Hu, D. Sun, Engineering the pore environment of metal–organic framework membranes via modification of the secondary building unit for improved gas separation, J. Mater. Chem. A 8(26) (2020) 13132-13141. https://doi.org/10.1039/C9TA13547B.
[33] S. Li, W. Gu, Y. Sun, D. Zou, W. Jing, Perforative pore formation on nanoplates for 2D porous MXene membranes via H_2O_2 mild etching, Ceramics International (2021).

606 [34] C. Yu, B. Zhang, F. Yan, J. Zhao, J. Li, Engineering nano-porous graphene oxide by hydroxyl
607 radicals, Carbon 105(-) (2016) 291-296.
608 [35] G. Jiang, Y. Liu, Y. Wu, W. Xu, Q. Kong, C. Zhang, Transmission and radiation of acoustic oblique
609 incident through tube arrays based on phononic crystals theory, Appl. Acoust. 116 (2017) 117-126.
610 https://doi.org/https://doi.org/10.1016/j.apacoust.2016.09.020.
611 [36] Y. Wei, Z. Yang, L. Wang, Y. Yu, H. Yang, H. Jin, P. Lu, Y. Wang, D. Wu, Y. Li, C.Y. Tang, Facile ZIF–8
612 nanocrystals interlayered solvent–resistant thin–film nanocomposite membranes for enhanced
613 solvent permeance and rejection, J. Membr. Sci. 636 (2021).
614 https://doi.org/10.1016/j.memsci.2021.119586.
615 [37] X. Song, L. Wang, C.Y. Tang, Z. Wang, C. Gao, Fabrication of carbon nanotubes incorporated
616 double-skinned thin film nanocomposite membranes for enhanced separation performance and
617 antifouling capability in forward osmosis process, Desalination 369 (2015) 1-9.
618 https://doi.org/https://doi.org/10.1016/j.desal.2015.04.020.
619 [38] C. Xing, J. Han, X. Pei, Y. Zhang, J. He, R. Huang, S. Li, C. Liu, C. Lai, L. Shen, A.K. Nanjundan, S.
620 Zhang, Tunable graphene oxide nanofiltration membrane for effective dye/salt separation and
621 desalination, ACS Appl. Mater. Interfaces 13(46) (2021) 55339-55348.
622 https://doi.org/10.1021/acsami.1c16141.
623 [39] S. Zhao, Y. Wang, J. Dong, C.-T. He, H. Yin, P. An, K. Zhao, X. Zhang, C. Gao, L. Zhang, J. Lv, J.
624 Wang, J. Zhang, A.M. Khattak, N.A. Khan, Z. Wei, J. Zhang, S. Liu, H. Zhao, Z. Tang, Ultrathin metal–
625 organic framework nanosheets for electrocatalytic oxygen evolution, Nat. Energy 1(12) (2016).
626 https://doi.org/10.1038/nenergy.2016.184.
627 [40] M. Hu, B. Mi, Enabling graphene oxide nanosheets as water separation membranes, Environ.
628 Sci. Technol. 47(8) (2013) 3715-23. https://doi.org/10.1021/es400571g.
629 [41] G. Zou, H. Hou, G. Zhao, P. Ge, D. Yin, X. Ji, N-rich carbon coated $CoSnO_3$ derived fromin
630 situconstruction of a Co–MOF with enhanced sodium storage performance, J. Mater. Chem. A 6(11)
631 (2018) 4839-4847. https://doi.org/10.1039/c7ta10448k.
632 [42] X. Hang, Y. Xue, Y. Cheng, M. Du, L. Du, H. Pang, From Co-MOF to CoNi-MOF to Ni-MOF: A facile
633 synthesis of 1D micro-/nanomaterials, Inorg. Chem. 60(17) (2021) 13168-13176.
634 https://doi.org/10.1021/acs.inorgchem.1c01561.
635 [43] H. Zhang, T. Wang, A. Sumboja, W. Zang, J. Xie, D. Gao, S.J. Pennycook, Z. Liu, C. Guan, J. Wang,
636 Integrated hierarchical carbon flake arrays with hollow P-doped $CoSe_2$ nanoclusters as an advanced
637 bifunctional catalyst for Zn-Air batteries, Adv. Funct. Mater. 28(40) (2018).
638 https://doi.org/10.1002/adfm.201804846.
639 [44] Y. Wang, Y. Liu, H. Wang, W. Liu, Y. Li, J. Zhang, H. Hou, J. Yang, Ultrathin NiCo-MOF nanosheets
640 for high-performance supercapacitor electrodes, ACS Appl. Energy Mater. 2(3) (2019) 2063-2071.
641 https://doi.org/10.1021/acsaem.8b02128.
642 [45] J.-J. Han, Q.-Y. Zhang, M.-Y. Huang, Y. Chen, X. Yan, W.-Z. Lang, Two-dimensional WS_2
643 membranes constructed on different substrates for efficient dye desalination, Desalination 480
644 (2020). https://doi.org/10.1016/j.desal.2020.114380.
645 [46] A. Schneemann, V. Bon, I. Schwedler, I. Senkovska, S. Kaskel, R.A. Fischer, Flexible metal–organic
646 frameworks, Chem. Soc. Rev. 43(16) (2014) 6062-6096.
647 [47] S. Yuan, J. Peng, B. Cai, Z. Huang, A.T. Garcia-Esparza, D. Sokaras, Y. Zhang, L. Giordano, K.
648 Akkiraju, Y.G. Zhu, R. Hubner, X. Zou, Y. Roman-Leshkov, Y. Shao-Horn, Tunable metal hydroxide-
649 organic frameworks for catalysing oxygen evolution, Nat. Mater. 21(6) (2022) 673-680.
650 https://doi.org/10.1038/s41563-022-01199-0.
651 [48] H. Wang, X. Chen, Y. Qi, L. Huang, C. Wang, D. Ding, X. Xue, Aggregation-induced emission (AIE)-
652 guided dynamic assembly for disease imaging and therapy, Adv. Drug Deliv. Rev. 179 (2021) 114028.
653 https://doi.org/https://doi.org/10.1016/j.addr.2021.114028.
654 [49] E. Hoenig, S.E. Strong, M. Wang, J.M. Radhakrishnan, N.J. Zaluzec, J.L. Skinner, C. Liu, Controlling
655 the structure of MoS_2 membranes via covalent functionalization with molecular spacers, Nano Lett.
656 20(11) (2020) 7844-7851. https://doi.org/10.1021/acs.nanolett.0c02114.

[50] X. Xie, C. Chen, N. Zhang, Z.-R. Tang, J. Jiang, Y.-J. Xu, Microstructure and surface control of MXene films for water purification, Nat. Sustain. 2(9) (2019) 856-862. https://doi.org/10.1038/s41893-019-0373-4.
[51] J. Ding, H. Zhao, B. Xu, H. Yu, Biomimetic sustainable graphene ultrafast-selective nanofiltration membranes, ACS Sustain. Chem. Eng. 8(24) (2020) 8986-8993. https://doi.org/10.1021/acssuschemeng.0c01568.
[52] L. Ding, D. Xiao, Z. Lu, J. Deng, Y. Wei, J. Caro, H. Wang, Oppositely charged $Ti_3C_2T_x$ Mxene membranes with 2D nanofluidic channels for osmotic energy harvesting, Angew. Chem. Int. Ed. 59(22) (2020) 8720-8726. https://doi.org/https://doi.org/10.1002/anie.201915993.
[53] C.L. Ritt, J.R. Werber, A. Deshmukh, M. Elimelech, Monte carlo simulations of framework defects in layered two-dimensional nanomaterial desalination membranes: Implications for permeability and selectivity, Environ. Sci. Technol. 53(11) (2019) 6214-6224. https://doi.org/10.1021/acs.est.8b06880.
[54] Z. Wang, Q. Tu, S. Zheng, J.J. Urban, S. Li, B. Mi, Understanding the aqueous stability and filtration capability of MoS_2 membranes, Nano Lett. 17(12) (2017) 7289-7298. https://doi.org/10.1021/acs.nanolett.7b02804.
[55] G. Yang, D. Liu, C. Chen, Y. Qian, Y. Su, S. Qin, L. Zhang, X. Wang, L. Sun, W. Lei, Stable Ti_3C_2Tx MXene–boron nitride membranes with low internal resistance for enhanced salinity gradient energy harvesting, ACS Nano 15(4) (2021) 6594-6603. https://doi.org/10.1021/acsnano.0c09845.
[56] Y. Liu, X.-p. Wang, Z.-a. Zong, R. Lin, X.-y. Zhang, F.-s. Chen, W.-d. Ding, L.-l. Zhang, X.-m. Meng, J. Hou, Thin film nanocomposite membrane incorporated with 2D-MOF nanosheets for highly efficient reverse osmosis desalination, J. Membr. Sci. 653 (2022) 120520. https://doi.org/https://doi.org/10.1016/j.memsci.2022.120520.
[57] L. Wang, X. Song, T. Wang, S. Wang, Z. Wang, C. Gao, Fabrication and characterization of polyethersulfone/carbon nanotubes (PES/CNTs) based mixed matrix membranes (MMMs) for nanofiltration application, Appl. Surf. Sci. 330 (2015) 118-125. https://doi.org/https://doi.org/10.1016/j.apsusc.2014.12.183.
[58] S. Majeed, D. Fierro, K. Buhr, J. Wind, B. Du, A. Boschetti-de-Fierro, V. Abetz, Multi-walled carbon nanotubes (MWCNTs) mixed polyacrylonitrile (PAN) ultrafiltration membranes, J. Membr. Sci. 403-404 (2012) 101-109. https://doi.org/https://doi.org/10.1016/j.memsci.2012.02.029.
[59] Y.H. See Toh, X.X. Loh, K. Li, A. Bismarck, A.G. Livingston, In search of a standard method for the characterisation of organic solvent nanofiltration membranes, J. Membr. Sci. 291(1-2) (2007) 120-125. https://doi.org/10.1016/j.memsci.2006.12.053.
[60] L. Chen, G. Shi, J. Shen, B. Peng, B. Zhang, Y. Wang, F. Bian, J. Wang, D. Li, Z. Qian, G. Xu, G. Liu, J. Zeng, L. Zhang, Y. Yang, G. Zhou, M. Wu, W. Jin, J. Li, H. Fang, Ion sieving in graphene oxide membranes via cationic control of interlayer spacing, Nature 550(7676) (2017) 380-383. https://doi.org/10.1038/nature24044.
[61] L. Wang, D. Rehman, P.-F. Sun, A. Deshmukh, L. Zhang, Q. Han, Z. Yang, Z. Wang, H.-D. Park, J.H. Lienhard, Novel positively charged metal-coordinated nanofiltration membrane for lithium recovery, ACS Appl. Mater. Interfaces 13(14) (2021) 16906-16915.
[62] K. Rasool, R.P. Pandey, P.A. Rasheed, S. Buczek, Y. Gogotsi, K.A. Mahmoud, Water treatment and environmental remediation applications of two-dimensional metal carbides (MXenes), Mater. Today 30 (2019) 80-102.
[63] M. Fathizadeh, W.L. Xu, F. Zhou, Y. Yoon, M. Yu, Graphene oxide: a novel 2‐dimensional material in membrane separation for water purification, Adv. Mater. Interfaces 4(5) (2017) 1600918.
[64] L. Long, C. Wu, Z. Yang, C.Y. Tang, Carbon nanotube interlayer enhances water permeance and antifouling performance of nanofiltration membranes: Mechanisms and experimental evidence, Environ. Sci. Technol. 56(4) (2022) 2656-2664. https://doi.org/10.1021/acs.est.1c07332.
[65] L. Huang, S. Huang, S.R. Venna, H. Lin, Rightsizing nanochannels in reduced graphene oxide membranes by solvating for dye desalination, Environ. Sci. Technol. 52(21) (2018) 12649-12655. https://doi.org/10.1021/acs.est.8b03661.

[66] L. Zhu, H. Wang, J. Bai, J. Liu, Y. Zhang, A porous graphene composite membrane intercalated by halloysite nanotubes for efficient dye desalination, Desalination 420 (2017) 145-157. https://doi.org/https://doi.org/10.1016/j.desal.2017.07.008.
[67] Y. Liu, X. Chen, Y. Yang, Y. Feng, D. Wu, S. Mao, Activation of persulfate with metal–organic framework-derived nitrogen-doped porous Co@C nanoboxes for highly efficient p-Chloroaniline removal, Chem. Eng. J. 358 (2019) 408-418. https://doi.org/10.1016/j.cej.2018.10.012.